Chinese Chemical Letters 33 (2022) 1095–1099

Contents lists available at ScienceDirect

Chinese Chemical Letters

journal homepage: www.elsevier.com/locate/cclet

Plasma treated carbon paper electrode greatly improves the performance of iron-hydrogen battery for low-cost energy storage

Chuang Bai[a,b], Fandi Ning[a,b], Saifei Pan[a,b], Huihui Wang[b], Yali Li[a,b], Min Shen[b], Xiaochun Zhou[a,b,*]

[a] School of Nano-Tech and Nano-Bionics, University of Science and Technology of China, Hefei 230026, China
[b] Division of Advanced Nanomaterials, Suzhou Institute of Nano-tech and Nano-bionics, Chinese Academy of Sciences (CAS), Suzhou 215123, China

ARTICLE INFO

Article history:
Received 23 April 2021
Revised 26 May 2021
Accepted 2 July 2021
Available online 11 July 2021

Keywords:
Plasma modification
Carbon paper
Iron ion
Hydrogen
Hybrid battery

ABSTRACT

A novel iron-hydrogen battery system, whose Fe^{3+}/Fe^{2+} cathode circumvents slowly dynamic oxygen reduction reaction and anode is fed with clean and cordial hydrogen, is systematically investigated. The maximum discharge power density of the iron-hydrogen battery reaches to 96.0 mW/cm^2 under the room temperature. The capacity reaches to 17.2 Ah/L and the coulombic and energy efficiency are achieved to 99% and 86%, respectively, during the galvanostatic charge-discharge test. Moreover, stable cycling test is observed for more than 240 h and 100 cycles with the iron sulfate in the sulfuric acid solutions. It is found that air plasma treatment onto the cathode carbon paper can generate the oxygen-containing groups and increase the hydrophilic pores proportion to *ca*. 40%, enlarging nearly 6-fold effective diffusion coefficient and improving the mass transfer in the battery performance. The simple iron-hydrogen energy storage battery design offers us a new strategy for the large-scale energy storage and hydrogen involved economy.

In the past two decades, the renewable electricity generating capacity has increased greatly [1–4], but most of the renewable energy power generations, such wind and solar power, have the characteristics of uncertainty and discontinuity [5–7]. Thus the stable and efficient energy storage methods are needed for energy conversion and harvest [8,9]. To meet these needs, the redox flow batteries (RFBs) and the proton exchange membrane fuel cells (PEMFCs) have attracted wide attention. RFBs are attractive energy storage technologies because of the property to be independent modular designed in terms of power and capacity [10]. However, RFBs application is limited by metal deposition [11], uneconomical metal ions and organic ligands [12] and low electrolyte concentration [13], *etc.* For example, the well-known vanadium redox flow battery is of high cost owing to the usage of expensive vanadium [14]. The latter, PEMFCs, are eye-catching because of the clean raw materials and high energy density (current reach to 135 Wh/kg) [15,16] even compared to excellent VRFBs (< 40 Wh/kg) [17–19]. But the kinetics of the oxygen reduction are ~5 orders of magnitude slower than hydrogen oxidation kinetics [20,21] and the load of Pt on the oxygen side is 4 times that on the hydrogen side (total Pt loading of 0.125 mg/cm^2 by 2020 is a target of the U.S. Department of Energy) [22]. On the contrary, the anode side of PEMFCs for hydrogen oxidation could achieve high performance and high energy conversion efficiency at very low loading of precious metal catalyst.

The large-scale energy storage with low cost can be realized with combining the advantages of RFBs and PEMFCs and omit the disadvantages of them. Moreover, RFBs share many common components with PEMFCs such as proton exchange membranes, electrodes, flow field plates and bipolar plates [10]. Then, the lower toxicity and cheaper Fe^{2+}/Fe^{3+}, and clean and highly active H_2/H^+ redox couples are chosen to be assembled a hybrid system, the iron-hydrogen energy storage battery (IHESB). The half reactions on cathode and anode side are

$$\text{Cathode: } 2Fe^{3+}_{(aq)} + 2e^- \rightarrow 2Fe^{3+}_{(aq)} \quad E_0 = 0.77 \text{ V } \textit{versus} \text{ RHE} \tag{1}$$

$$\text{Anode: } H_2 \rightarrow 2H^+ + 2e^- \quad E_0 = 0.00 \text{ V } \textit{versus} \text{ RHE} \tag{2}$$

Then the overall reaction is

$$2Fe^{3+}_{(aq)} + H_2 \rightarrow 2Fe^{3+}_{(aq)} + 2H^+ \quad E_0 = 0.77 \text{ V } \textit{versus} \text{ RHE} \tag{3}$$

Since the iron ions and hydrogen are economical and non-toxic compared to common flow battery systems such as vanadium, bromine, chlorine, lead and chromium [23,24], and just a small amount of catalyst is needed only on hydrogen oxidation reaction,

* Corresponding author.
E-mail address: xczhou2013@sinano.ac.cn (X. Zhou).

https://doi.org/10.1016/j.cclet.2021.07.008
1001-8417/

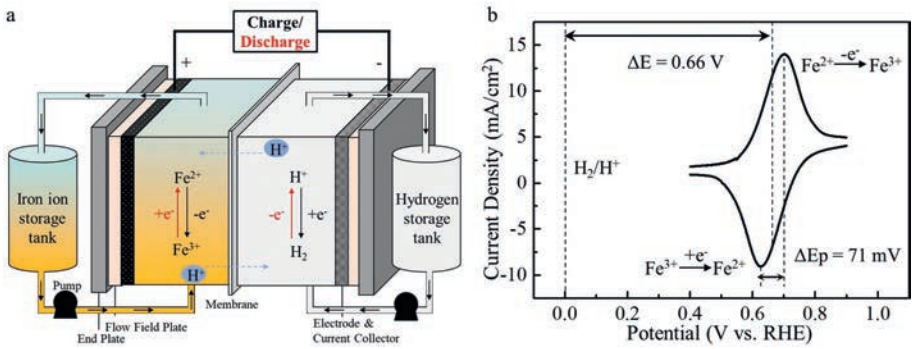

Fig. 1. (a) A schematic representation of the iron-hydrogen energy storage battery (IHESB). (b) Cyclic voltammogram of ferric sulfate (scan rate is 2 mV/s, in 0.4 mol/L $Fe_2(SO_4)_3$ with 1 mol/L H_2SO_4 electrolyte).

the IHESB combines the advantages of RFBs and PEMFCs and is a competitive candidate for energy storage and conversion.

Plasma treatment has been recognized as an efficient method to influence the material surface energy, wettability, and can introduce hydroxyl and carbonyl groups and increase surface roughness with choosing gas [25,26]. Moreover, plasma is popular because of its convenience and not involving any toxic chemicals [27–31] compared with thermal oxidation [32], acid treatment [33], and other chemical oxidation methods [34], *etc*. Because of oxygen-containing function groups facilitate the Fe (II)/Fe (III) redox reactions [35,36], air plasma is selected to modify the carbon paper cathode electrode which is beneficial to increase the power density and energy efficiency.

In this work, no catalyst such as PtIr alloy on Vulcan XC-72 [37] is used in Fe(II)/Fe(III) redox reactions, reducing the cost. And with hydrogen directly pass through the gas diffusion layer instead of bubbling hydrogen through the liquid [38–40], the liquid iron plus hydrogen gas system avoids the influence of crossover. The high performance IHESBs are assembled by using a series of carbon paper electrodes with air plasma modification. The discharge maximum power density of the battery is improved from 4.4 mW/cm^2 with non-treatment electrode to 96.0 mW/cm^2 with electrode under plasma treatment. And the capacity density of the battery can reach 15.5 Ah/L from 11.7 Ah/L at a galvanostatic current density of 60 mA/cm^2, and CE is close to 100%. The reasons for the improved performance are the increase of hydrophilicity, the introduction of oxygen-containing functional groups, and the enhancement of mass transfer. After 100 cycles of continuous cycling during 240 h, CE is almost unchanged and remaining above 99% and VE and EE decrease less than 14%, which shows a good cycling performance.

The schematic structure of the IHESB is shown in Fig. 1a and the components details can be seen in Fig. S1 (Supporting information). It mainly consists of electrolyte storage tanks, end plates, flow field plates, electrodes, current collector plates and proton exchange membrane. The cathode is the liquid ferric sulfate in sulfuric acid and the anode is hydrogen gas. When the battery is charging, the divalent iron ions on the cathode are oxidized to the trivalent state, and the protons migrate from the cathode to the anode and are reduced to the hydrogen. When the battery is discharging, the hydrogen on the anode is oxidized to the protons, and the protons migrate to the cathode through the proton exchange membrane, and the ferric ions on the cathode are reduced to divalent iron ions.

Fig. 1b shows the cyclic voltammetry spectrum of the ferric sulfate and the potential of the hydrogen electrode. The ferric sulfate is dissolved in the sulfuric acid solution, the cathode is used as the working electrode, and the anode is used as the counter electrode and the reference electrode. The half wave potential of ferric sulfate catholyte is 0.66 V *versus* hydrogen anode, which is smaller than the theoretical value (E_0 = 0.77 V). The relatively low electrode reaction potential is because of the non-ideal hydrogen reference electrode and the open circuit voltage is near to the theoretical value during the battery test section. And the peak potential difference between oxidation and reduction of iron sulfate at a sweep rate of 2 mV/s is only 71 mV, which is a *quasi*-reversible electrode reaction process, and is beneficial for high energy efficiency of the battery.

Fig. 2a shows the schematic diagram of plasma treatment process. The surface morphology and composition of the carbon paper remain unchanged after simple air plasma treatment, but the surface changes from hydrophobic to hydrophilic, and the proportion of hydrophilic oxygen-containing groups is greatly increased. After plasma treatment for different periods of time, the SEM spectra of the carbon papers are shown in Figs. 2b-g. The general morphology, diameter, and distribution of the carbon fibers in the carbon paper were basically unchanged, but according to the upper right embedded SEM spectra for small scale, the surface of the carbon fibers in the carbon paper became rougher after long-term plasma treatment. Goniometry was conducted using DI water as the working solvent. And the embedded images in the lower left corner of Figs. 2b-g show that the untreated carbon paper was quite hydrophobic with a contact angle of 125°. But after the air plasma treatment, the surface of the carbon paper became completely hydrophilic and the contact angle could not be recorded because that the surface of carbon paper became wet instantly as it touted the droplet. The increased hydrophilicity will facilitate the penetration of cathode solution and mass transfer, and improve the power density and discharge performance.

To explain the change in hydrophilic properties, an XPS study has been conducted to exactly identify the surface chemical state of carbon papers before and after the surface treatment. The change of XPS data and element contents are shown in Fig. S2 (Supporting information) in the supporting information and the ratio of functional groups [33,34,41] can be obtained from the C 1s fine XPS spectrums. The changes with contents of carbon functional groups are shown in Fig. 2c. The ratio of C-C groups decreases and maintains to around 65%. The ratio of C-OR groups also decreases while the C=O and COOH hydrophilic groups newly appear and increase to approximately 20%. The type and content of functional groups are the essential reasons for the changes in carbon paper properties.

Untreated carbon paper and the one treated with air plasma for 10 min are obtained and the discharge performance of the assembled IHESB is shown in Fig. 2d. The peak power density of IHESB with the use of untreated carbon paper is only 4.4 mW/cm^2, but applied with carbon paper treated with air plasma for 10 min, the limit current density and peak power density reaches to 355

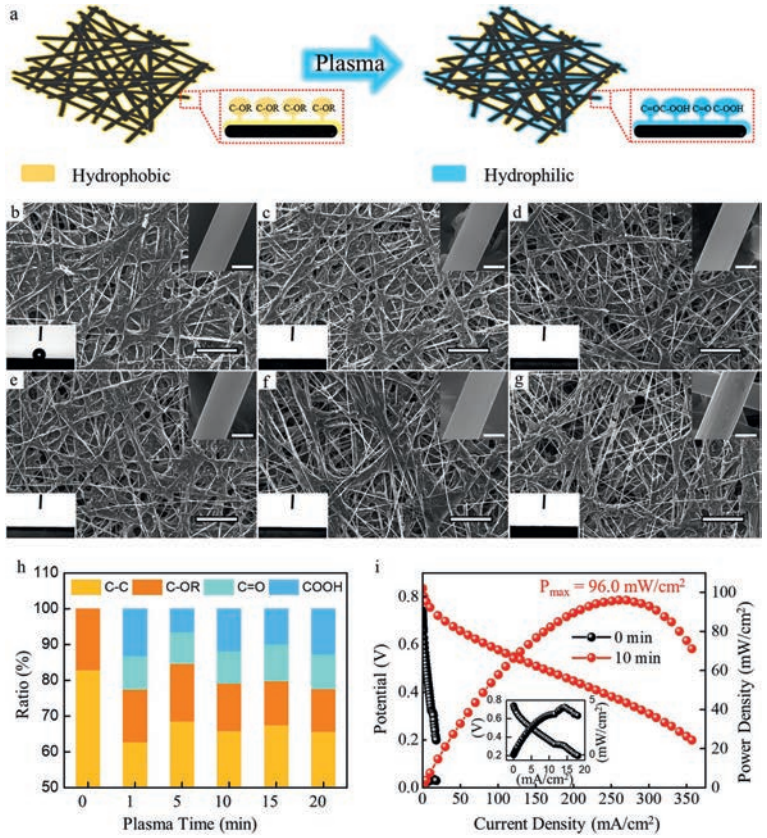

Fig. 2. (a) Schematic diagram of carbon paper plasma treatment process. (b-g) SEM spectrograms of carbon papers treated by air plasma for 0-20 min (The size of ruler is 300 μm). The size of ruler of embedded images in the upper right corner is 5 μm and embedded images in the lower left corner are the corresponding surface contact angle images. (h) The ratio trends of carbon functional groups with increasing plasma treatment time. (i) IHESB discharge performances applied with untreated carbon paper cathode and the one treated with air plasma for 10 min.

mA/cm^2 and 96.0 mW/cm^2, respectively. Besides, the open circuit voltage is increased from 0.74 V to 0.84 V, but the voltage drops rapidly under small current density, which shows the high circuit voltage over 0.77 V may be due to the electrochemical reaction of newly introduced hydrophilic groups and impurities on the plasma treated carbon paper electrode. The enhanced peak power density is higher than the previous report at 70 mW/cm^2 [42]. It is worth mentioning that iron sulfate instead of ferric chloride was used as the electrolyte, less corrosive (Fig. S3 in Supporting information) [37] and non-toxic to platinum catalyst on anode [43] and more suitable for practical applications.

Fig. 3a shows the galvanostatic charge and discharge property for the carbon paper before and after plasma modification. All samples are tests at least for 5 cycles (Fig. S4 in Supporting information) and exhibit almost the same charge and discharge capacity without undesirable capacity loss which results the excellent performance with coulombic efficiency (CE) of above 99%. The discharge capacity of the battery is 11.7 Ah/L without plasma treatment. As the plasma time increases, the discharge capacity of the battery reaches the maximum value of 15.5 Ah/L at 10 min. But as the plasma time further increases, the performance of the battery gradually decreases. The voltage efficiency (VE) and energy efficiency (EE) of battery reflected in Fig. 3b also have a similar trend. The performance degradation caused by prolonging the plasma time may be due to the minor damage of the carbon fiber in the carbon paper. The VE and EE of the battery when the carbon paper electrode is not processed are only 52%, but the battery composed of 10 min treatment can reach 70% efficiency.

The rate capability is a merit for practical application, and the galvanostatic charge and discharge curves at different current densities of the IHESB is shown in Fig. 3c. With the increase of charge and discharge current density, the discharge capacity of the battery slightly decreases from 17.2 Ah/L at 10 mA/cm^2 to 15.5 Ah/L at 60 mA/cm^2. The theoretical capacity is 21.4 Ah/L with using 0.4 mol/L $Fe_2(SO_4)_3$ and the capacity can be increased with future optimization of iron ion concentration. Meanwhile, the CE, VE and EE of IHESB under different current density are presented in Fig. 3d. It shows that the CE of the battery is kept at above 99% in the current density range of 10 mA/cm^2 to 60 mA/cm^2, and the VE and EE are only reduced from 86% to 70%. The VE and EE decreases are caused by the increased ohmic loss which uplift the charge curve and descent the discharge curve as the increasing current density. The large current density working range and high efficiencies are beneficial to the practical energy storage applications. The cycling stability is also a serious concern for energy storage batteries.

Fig. 3e shows the long-term charge-discharge cycling test at the current density of 50 mA/cm^2 and the cycling curves are shown in Figure S5a. The battery's discharge capacity density has been maintained at 15.5 Ah/L during 100 cycles for more than 240 h, and the CE is basically maintained at above 99% without attenuation. The inset graph displays that the 1st charge and discharge profile completely coincides with the 50th one, but there is a slight deviation from the 100th profile. As shown in Fig. S3b, there is obvious crossover liquid on the anode surface, which comes from the cathode electrolyte. The penetration of the liquid will damage the property of the Nafion membrane and reduce the battery performance, which is blame for the decrease in VE and EE and consistent with literature reports [8,44–46].

In order to explain the hydrophilicity and surface groups changes on the electrochemical activity and battery performance,

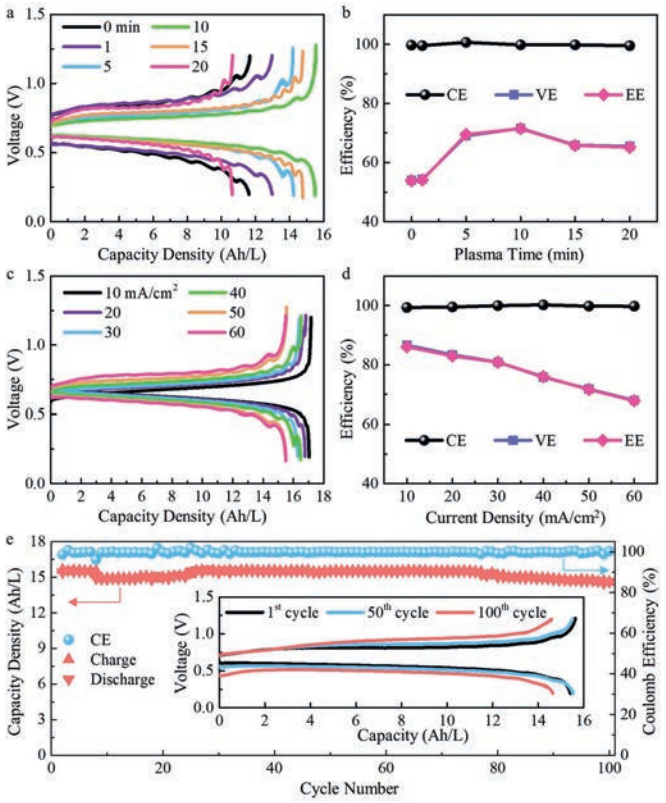

Fig. 3. (a) The charge and discharge curves and (b) efficiencies of IHESB with carbon paper treated with plasma for different times (test under 50 mA/cm^2). (c) The charge and discharge curves and (d) efficiencies of IHESB under different current densities. Carbon paper treated with plasma at 10 min for anode electrode was used. (e) The battery cycling performance under 50 mA/cm^2. The curves of the 1st, 50th and 100th cycles are presented in the embedded image. Carbon paper treated with plasma at 10 min for cathode electrode was used.

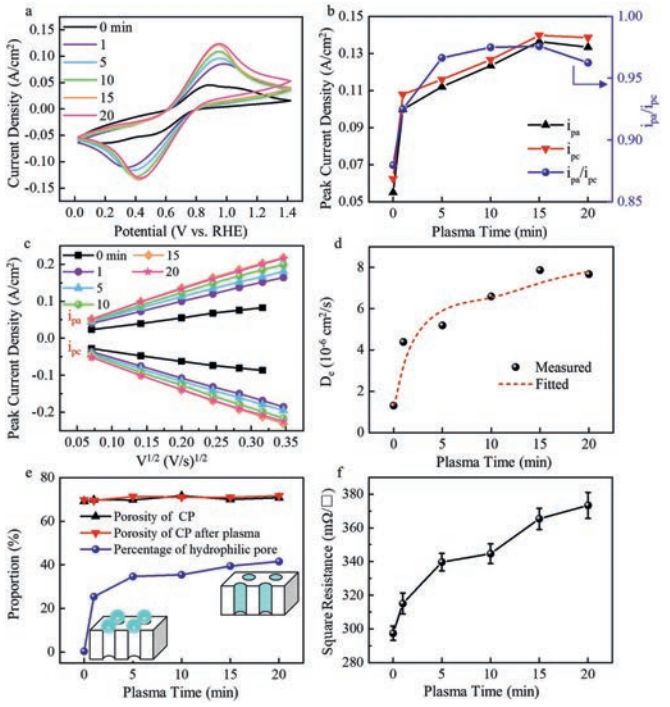

Fig. 4. (a) Cyclic voltammograms of iron ion. Scan rate: 40 mV/s. (b) Peak current densities and ratio of redox peak current densities for iron ion used with carbon paper electrode treated with plasma after different times. Scan rate: 40 mV/s. (c) Peak current densities for iron ion *versus* the square root of scan rate. Scan rate: 5-120 mV/s. Conditions: 0.4 mol/L $Fe_2(SO_4)_3$ in 1 mol/L H_2SO_4 electrolyte; WE: carbon paper electrode treated with plasma after different times, CE: Pt wire, RE: Ag/AgCl. (d) The measured and fitted effective diffusion coefficients of Fe^{3+} on the carbon paper electrode treated with plasma for different times. (e) Changes of porosity and percentage of hydrophilic pores for carbon paper with and without plasma treatment. (f) The square resistances of carbon paper electrode treated with plasma for different times.

the characterizations of carbon paper before and after plasma treatment are performed. The carbon paper is used as the working electrode, and the Ag/AgCl and the platinum wire electrode are used as the reference electrode and the counter electrode, respectively. The cyclic voltammetry reveals that the Fe^{2+}/Fe^{3+} redox current density gradually increases with the plasma treatment time while the oxidation peak voltage gradually increases, and the reduction peak voltage gradually decreases as shown in Fig. 4a. The redox current density increase phenomenon is more obvious in Fig. 4b and the ratio of peak redox current density (i_{pa}/i_{pc}) approaches to 1 after being treated with plasma. The changes prove that the modified carbon paper electrode has better electrochemical activity and reversibility.

Plot the peak redox current density *versus* the square root of the scan rate, and it can be found that there is an obvious linear relationship in Fig. 4c, which suggests that the Fe(II)/Fe(III) redox reaction on the carbon paper electrode is a diffusion-controlled process. Calculated with the Randles-Sevcik equation for *quasi*-reversible process [47], the effective diffusion coefficient (D_e) of iron ion on the carbon paper electrode surface can be obtained. The results in Fig. 4d shows that D_e of Fe^{3+} increases with the increase of plasma time from 1.3 cm^2/s to 7.7 $\times$ 10^{-6} cm^2/s, which proves that the air plasma treatment greatly promotes the mass transfer efficiency. The D_e of Fe^{2+} also shows a similar growth trend and can be seen in Fig. S6e (Supporting information).

For the same examination on the glassy carbon electrode surface, plasma does not change the diffusion coefficient of Fe^{3+} on the electrode surface (Fig. S6 in Supporting information). In addition, effective diffusion coefficient is related to the porosity of electrode according to previous work [48], the porosities of carbon papers are measured using the method in Fig. S7 (Supporting information) and the results are shown in Fig. 4e. As increasing the plasma time, the porosity of the carbon paper almost remains the same but the proportion of hydrophilic pores increases to *ca.* 40% and then remains stable. And the effective diffusion coefficient could be calculated through the section SI-8 (Supporting information). The fitting curve (red dotted line in Fig. 4d) is in good agreement with the experimental data and this change in the D_e increases the mass transfer and improves the power density and capacity. As for the square resistance test shown in Fig. 4f, the increase in plasma time will increase the square resistance of the carbon paper, which is the reason for the battery performance decrease as the plasma time rises to more than 10 min. Longtime plasma treatment damages the structure of the treated material because of the high-energy species [49], and it is necessary to choose the appropriate modifying time [50]. Moreover, the treated material has the limitation of shape and size due to the limitation of the plasma instrument cavity, and plasma technology has timeliness [51,52]. Therefore, the stacks production and combing the plasma pretreatment and other active material coating [53,54] are meaningful and those studies are undertaken.

The performance of the iron-hydrogen battery is enhanced by the air plasma treatment and the enhance of mass transfer on the carbon paper cathode is the reason of the improvment. A maximum discharge power of 96.0 mW/cm^2 was observed at room temperature and all the charge and discharge examinations show a high CE (close to 100%). Beside, an EE of 86% and capacity energy of 17.2 Ah/L is achieved at 10 mA/cm^2 for 0.4 mol/L $Fe_2(SO_4)_3$ with

1 mol/L H_2SO_4. And stable cycling was measured at 50 mA/cm^2 for 240 h and 100 cycles with no obvious perfomance loss. Further optimization of cathode solution composition, cathode electrode material and cell structure will be conducive to the battery performance and practical applications.

Declaration of competing interest

The authors report no declarations of interest.

Acknowledgments

The authors are grateful for financial support granted by National Key R&D Program of China (No. 2020YFB1505704), Dongyue Polymer Material Company of Dongyue Federation, State Key Laboratory of Fluorinated Functional Membrane Materials (Dongyue Group institute) and Dongyue Future Hydrogen Energy Materials Company. This work was sponsored by the Collaborative Innovation Center of Suzhou Nano Science and Technology.

Supplementary materials

Supplementary material associated with this article can be found, in the online version, at doi:10.1016/j.cclet.2021.07.008.

References

[1] M.S. Ziegler, J.M. Mueller, G.D. Pereira, et al., Joule 3 (2019) 2134–2153.
[2] S. Pang, X. Wang, P. Wang, Y. Ji, Angew. Chem. Int. Ed. 60 (2021) 5289–5298.
[3] M. Ferrara, Y.-M. Chiang, J.M. Deutch, Joule 3 (2019) 2585–2588.
[4] J. Zhang, X. Sheng, Z. Ding, et al., Sci. Bull. 66 (2021) 164–169.
[5] T. Liu, X. Wei, Z. Nie, V. Sprenkle, W. Wang, Adv. Energy Mater. 6 (2016) 1501449.
[6] J. Luo, B. Hu, C. Debruler, T.L. Liu, Angew. Chem. Int. Ed. 57 (2018) 231–235.
[7] X. Wei, W. Pan, W. Duan, et al., ACS Energy Lett. 2 (2017) 2187–2204.
[8] Y. Zhen, C. Zhang, J. Yuan, Y. Zhao, Y. Li, J. Power Sources 445 (2020) 227331.
[9] K. Gong, F. Xu, J.B. Grunewald, et al., ACS Energy Lett. 1 (2016) 89–93.
[10] Y. Shao, Y. Cheng, W. Duan, et al., ACS Catal. 5 (2015) 7288–7298.
[11] J. Noack, N. Roznyatovskaya, T. Herr, P. Fischer, Angew. Chem. Int. Ed. 54 (2015) 9776–9809.
[12] X. Wei, W. Xu, M. Vijayakumar, et al., Adv. Mater. 26 (2014) 7649–7653.
[13] J. Winsberg, T. Hagemann, T. Janoschka, M.D. Hager, U.S. Schubert, Angew. Chem. Int. Ed. 56 (2017) 686–711.
[14] C. Ding, H. Zhang, X. Li, T. Liu, F. Xing, J. Phys. Chem. Lett. 4 (2013) 1281–1294.
[15] H. Wang, C. Bai, T. Zhang, et al., ACS Appl. Mater. Inter. 12 (2020) 4473–4481.
[16] K. Wang, N. Li, Y. Yang, et al. , Chin. Chem. Lett. 32 (2021) 3159–3163.
[17] L. Li, S. Kim, W. Wang, et al., Adv. Energy Mater. 1 (2011) 394–400.
[18] S. Roe, C. Menictas, M. Skyllas-Kazacos, J. Electrochem. Soc. 163 (2015) A5023–A5028.
[19] K. Lourenssen, J. Williams, F. Ahmadpour, R. Clemmer, S. Tasnim, J. Energy Storage 25 (2019) 100844.
[20] D. Banham, S. Ye, ACS Energy Lett. 2 (2017) 629–638.
[21] L. Zhou, L. Chen, Z. Ding, et al., Nano Res. 14 (2020) 172–176.
[22] Multi-Year Research, Development, and Demonstration Plan, http://energy.gov/sites/prod/files/2016/10/f33/fcto_myrdd_fuel_cells.pdf.
[23] M.C. Tucker, K.T. Cho, A.Z. Weber, J. Power Sources 245 (2014) 691–697.
[24] K. Fatih, D.P. Wilkinson, F. Moraw, A. Ilicic, F. Girard, Electrochem. Solid-State Lett. 11 (2008) B11.
[25] N. Kasoju, L.T.B. Nguyen, A.R. Padalhin, et al., Techniques for modifying biomaterials to improve hemocompatibility, in: C.A. Siedlecki (Ed.), Hemocompatibility of Biomaterials for Clinical Applications, Woodhead Publishing Inc., Duxford, 2018, pp. 191–220.
[26] S. Dou, L. Tao, R. Wang, et al., Adv. Mater. 30 (2018) e1705850.
[27] X. Wu, H. Xu, P. Xu, et al., J. Power Sources 263 (2014) 104–109.
[28] B. Sun, M. Skyllas-Kazacos, Electrochim. Acta 37 (1992) 1253–1260.
[29] B. Sun, M. Skyllas-Kazacos, Electrochim. Acta 37 (1992) 2459–2465.
[30] R. Cheng, F. Zhang, M. Li, et al., Front. Chem. 7 (2019) 588.
[31] W. Xu, X. Sheng, H. Zhou, et al., Chem. Eng. J. 410 (2021) 128342.
[32] P.C. Ghimire, R. Schweiss, G.G. Scherer, et al., Carbon 155 (2019) 176–185.
[33] Y.J. Kim, H.J. Lee, S.W. Lee, B.W. Cho, C.R. Park, Carbon 43 (2005) 163–169.
[34] V. Datsyuk, M. Kalyva, K. Papagelis, et al., Carbon 46 (2008) 833–840.
[35] Y.K. Zeng, X.L. Zhou, L. An, L. Wei, T.S. Zhao, J. Power Sources 324 (2016) 738–744.
[36] E. Hollax, D.S. Cheng, Carbon 23 (1985) 655–664.
[37] M. Alon, A. Blum, E. Peled, J. Power Sources 240 (2013) 417–420.
[38] Y.K. Zeng, T.S. Zhao, X.L. Zhou, J. Zou, Y.X. Ren, J. Power Sources 352 (2017) 77–82.
[39] M.C. Tucker, A. Weiss, A.Z. Weber, J. Power Sources 327 (2016) 591–598.
[40] V. Watson, D. Nguyen, E.E. Effiong, E.E. Kalu, ECS Electrochem. Lett. 4 (2015) A72–A75.
[41] R. Nie, M. Miao, W. Du, et al., Appl. Catal. B 180 (2016) 607–613.
[42] M.C. Tucker, V. Srinivasan, P.N. Ross, A.Z. Weber, J. Appl. Electrochem. 43 (2013) 637–644.
[43] N. Garcia-Araez, V. Climent, P. Rodriguez, J.M. Feliu, Langmuir 26 (2010) 12408–12417.
[44] K. Marma, J. Kolli, K.T. Cho, J. Electrochem. En. Conv. Stor. 16 (2019) 011005.
[45] M. Skyllas-Kazacos, J. Power Sources 124 (2003) 299–302.
[46] T. Okada, Effect of ionic contaminants, in: W. Vielstich, A. Lamm, H.A. Gasteiger, H. Yokokawa (Eds.), Handbook of Fuel Cells - Fundamentals, Technology and Applications, John Wiley & Sons, Ltd., 2010, pp. 1721–1740.
[47] P. Zanello, in: Inorganic Electrochemistry: Theory, Practice and Application, The Royal Society of Chemistry, Ltd., 2003, pp. 49–136.
[48] X. Zhou, W. Ouyang, C. Liu, et al., J. Power Sources 158 (2006) 1209–1221.
[49] D. Wang, Y. Zou, L. Tao, et al., Chin. Chem. Lett. 30 (2019) 826–838.
[50] X. Guo, L. Xiao, P. Yan, et al., Chin. Chem. Lett. 32 (2021) 3491–3495.
[51] R.A. Lawton, C.R. Price, A.F. Runge, W.J. Doherty, S.S. Saavedra, Colloids and Surf. A 253 (2005) 213–215.
[52] S. Debnath, R. Ranade, S.L. Wunder, et al., J. Appl. Polym. Sci. 96 (2005) 1564–1572.
[53] J.Y. Meng, Y.Y. Wang, Adv. Mater. Res. 1015 (2014) 303–307.
[54] C.X. Wang, J.C. Lv, Y. Ren, et al., Appl. Surf. Sci. 359 (2015) 196–203.